DOI: 10.15480/882.9364

Eighth International Symposium on Marine Propulsors
smp'24, Berlin, Germany, March 2024

Quantifying the Influence of Gate Rudder System (GRS) Rudder Angle(s) on Propeller Cavitation

Çağatay Sabri Köksal[1], Ahmet Yusuf Gürkan[1], Batuhan Aktas[1], Uğur Oral Ünal[2], Patrick Fitzimmons[1], Noriyuki Sasaki[1], Emin Korkut[2], Mehmet Atlar[1]

[1]Department of Naval Architecture, Ocean & Marine Engineering, University of Strathclyde (UoS), Glasgow, United Kingdom
[2]Faculty of Naval Architecture and Ocean Engineering, Istanbul Technical University (ITU), Istanbul, Türkiye

ABSTRACT

The study is on the propeller cavitation extent analysis of a 90m coastal cargo ship, M/V ERGE, overlaying Computational Fluid Dynamics (CFD) analyses and full-scale observation for the first time. The sea trials with M/V ERGE were performed before and after the first retrofit application of a Gate Rudder System (GRS) on this vessel as a pioneering alternative to its Conventional Rudder System (CRS), the aim of the H2020 Project GATERS. This study's objective is to explore the impact of the rudder angle(s) variations on the cavitation patterns of the GRS' propeller. The cavitation observations during the sea trials were conducted in the trial (ballast) loading conditions, and the gate rudder angle was 8 degrees. The cavitation extensions were monitored and recorded in real-time throughout the sea trials with a specially designed and installed submerged monitoring system at the ship's aft end. The full-scale CFD analyses comprised the same configurations of the trials set up. The outcome of the analyses concerning the cavitation in varying gate rudder angles demonstrated a reasonable correlation between the observed and predicted patterns. The study revealed that the rudder angle configuration of the GRS influences the cavitation characteristics. These results also contribute to further understanding the cavitation dynamics and extension of the GRS propeller in full-scale for the first time, hence offering valuable insights into the design and optimisation process of this novel propulsion system, GRS.

Keywords

Cavitation observation, sea trials, numerical prediction, full-scale Computational Fluid Dynamics (CFD) analyses.

1 INTRODUCTION

The Gate Rudder System (GRS) enables a proven and remarkable reduction in fuel consumption (GATERS 2023 and 2024) as well as improvements in manoeuvrability (Carchen et al 2021), seakeeping (Sasaki et al 2019, Köksal et al 2022), cavitation pattern (Özsayan et al 2023, Köksal et al 2023a) and underwater radiated noise (Santic et al 2023, Köksal et al 2023b) characteristics, thus contributing to energy efficiency and water-borne noise mitigation. The GRS configuration is the arrangement of symmetrical rudder blades on either side (i.e., port and starboard) of the propeller. The design parameters of the GRS are tens of variables (Gürkan et al 2023a, Gürkan et al 2023b) including but not limited to the rudder angle(s). The fact remains that the adjustable rudder angle, apart from being one of the design variables, provides an adaptive configuration based on varying voyage conditions, such as the ship's draft and speed, relative wind speed and state of the sea to set the optimum rudder angle(s). As part of the EU H2020 Project GATERS activities (The EC - H2020 Project GATERS: GATE Rudder System as a Retrofit for the Next Generation Propulsion and Steering of Ships. Project ID 860337, 2021), a comparison has been made on the propeller's rotation rate (N), thrust (T), torque (Q) and delivered power (P_D), cavitation number (σ), advance coefficient (J) and wake fraction (w) obtained by experiments (EFD), numerical analyses (CFD) and sea trials of the GATERS target ship (M/V ERGE, a 90 m and 7421 DWT general cargo vessel). The ultimate objective of the present study is to quantify the effect of varying GRS rudder angles (i.e., 0, 5 and 8 degrees) on the propeller's cavitation pattern to complement the previously reported study investigating the effect of varying rudder angles on M/V ERGE's powering performance (Köksal et al 2023c).

2 SEA TRIALS

The delivery sea trials of M/V ERGE with the CRS were carried out in the Yellow Sea, China, in February 2010. The first sea trials of the same ship within the GATERS project with the existing CRS were performed in January 2023. M/V ERGE drydocked after the sea trials and retrofitted, changing the propeller, retracting steering and installing new steering gears and the GRS, and the last sea trials following the retrofit were conducted in May 2023. The sea trial area before and after the retrofit was Marmara Sea, Türkiye, and the trials campaign included the measurements of ship speed, shaft power, hull performance in varying engine loading conditions and manoeuvring tests as well as an underwater radiated noise (URN) survey.

2.1 Measurements and Cavitation Observation

The sea trials data such as N and Q were collected using an onboard monitoring system. The ship's location and fuel consumption were recorded and monitored in real-time using a GPS device and a flowmeter, respectively. An anemometer was used to record the wind speed and direction, and a wave buoy was deployed in the sea trial area to obtain significant wave height and the average wave period. Sea state level was observed to be less than Beaufort 2 during the sea trials; hence, no corrections were applied to the result of the measurements given in Table 1.

Table 1. The result of the measurements by sea trials in May 2023, and extracted coefficients (*σ*, *J*) in varying engine loads.

V_S (kn)	10.14	10.81	11.93	12.22
N (RPM)	107.1	116.9	130.5	136.7
Q (kN-m)	56.53	66.01	82.84	89.61
P_D (kW)	634.1	808.1	1131.7	1282.4
σ	5.706	4.790	3.846	3.505
J	0.597	0.608	0.604	0.612

The cavitation number (σ) in correspondence to the ship speed (V_S) was determined based on the ambient pressure (p_0) and the propeller's speed (N) as given in Equation (1).

$$\sigma = \frac{p_0 - p_v + \rho g h_s}{0.5\rho(ND)^2} \tag{1}$$

p_v is the vapour pressure, ρ is the density of water, g is the acceleration due to gravity, and h_s is the shaft's immersion. The advance coefficient (J) was obtained by the torque identity, using the propeller's speed (N) and the torque (Q).

The cavitation observations were carried out in varying engine/propeller loading conditions within the sea trials, using a custom-made cavitation observation mechanism designed and built by the authors. The cavitation observation mechanism shown in Fig. 1 was attached to the aft end of the ship, M/V ERGE, and cavitation patterns were monitored and recorded during the trials in real time.

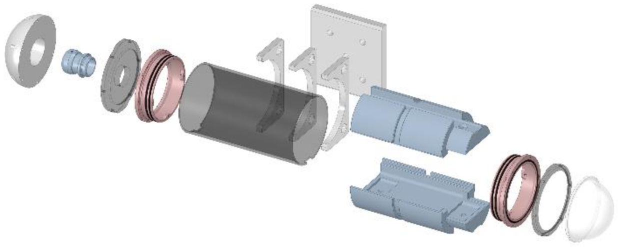

Figure 1. An exploded view of the cavitation observation mechanism, and its components, that is used in the sea trials.

The observed cavitation patterns based on the varying engine/propeller loading conditions, cavitation number (σ) and advance coefficient (J), are given in Fig. (2). The increase in N (i.e., V_S) corresponds to a decrease in σ and an increase in J, driven by the more significant increment in V_A compared to the increase in N. In Fig. (2), the cavitation is limited to tip vortex cavitation (TVC) at σ: 5.706, and the pattern turns into a solid form at σ: 4.790. A stable tip vortex cavitation formed at a lower radius than the tip radius at σ: 3.846. The initial strength form of tip vortex cavitation interacts with secondary weak TVC forming from the tip region at σ: 3.505 as shown in Fig. 2.

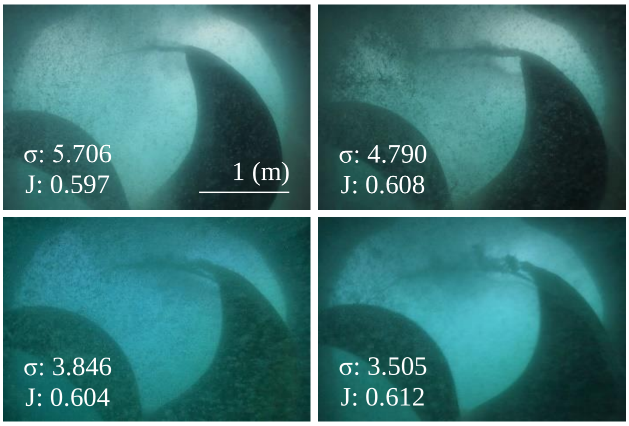

Figure 2. The observed cavitation pattern by sea trials under the various cavitation number (*σ*) and advance coefficient (*J*).

In Fig. (3), an enlarged view at σ: 3.505 is given along with the remarks (i.e., 1, 2 and 3). The first remark (1) points out a stable tip vortex cavitation forming at lower radius than tip radius, as being at σ: 3.846. The second remark (2) is on the breaking away tip sheet cavitation forming periodic discrete clumps. The last one (3) refers to discrete clumps collapsing and rebounding under the interaction of two forms, the strong and the weak one, of tip vortex cavitation.

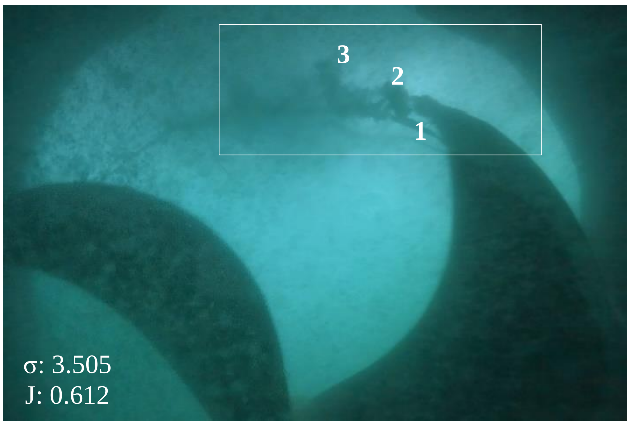

Figure 3. The observed cavitation pattern by sea trials along with highlighted remarks at *σ*: 3.505 and *J*: 0.612 (V_S: 12.22)[1].

2 NUMERICAL METHODS

The CFD calculations were carried out using the STAR-CCM+. The incompressible Reynolds-averaged Navier-Stokes (RANS) model was utilised in the numerical analyses with the SST (Shear Stress Transport) k-ω turbulence model based on the Boussinesq hypothesis (Tennekes and Lumley 1972). A segregated algorithm was used in conjunction with the finite-volume method (Blazek 2001) to solve the momentum and turbulent transport equations. The pressure-correction-based SIMPLE technique (Patankar and Spalding 1972) was used to couple the pressure and velocity fields. The spatial discretisation of the convective terms of the Navier-Stokes and turbulent

---

[1] Observing the GRS' propeller from upstream perspective.

transport equations was acquired with a second-order-upwind scheme (Davidson 2005), whilst a bounded central differencing scheme was used for the viscous terms. The divergence of the mixture velocity is zero for the incompressible flow. However, in the cavitating flow, cavity evaporation and condensation cause a volume dilation, and the divergence of the mixture velocity does not vanish. Therefore, the general form of the conservation equations, valid for incompressible and compressible flows, is expressed in Cartesian tensor notation as follows.

$$\frac{\partial \rho}{\partial t}+\frac{\partial\left(\rho u_i\right)}{\partial x_i}=0 \tag{2}$$

$$\begin{aligned}\frac{\partial\left(\rho u_i\right)}{\partial t}+\frac{\partial\left(\rho u_i u_j\right)}{\partial x_j}&=-\frac{\partial p}{\partial x_i}\\&+\frac{\partial}{\partial x_j}\left[\mu\left(\frac{\partial u_i}{\partial x_j}+\frac{\partial u_j}{\partial x_i}-\frac{2}{3}\delta_{ij}\frac{\partial u_l}{\partial x_l}\right)\right]+\frac{\partial\left(-\rho\overline{u_i' u_j'}\right)}{\partial x_j}\end{aligned} \tag{3}$$

ρ is the liquid density, u averaged velocity, p averaged static pressure, u' fluctuating velocity and δ_{ij} is the Kronecker delta. $\rho\overline{u_i' u_j'}$ denotes the Reynolds stress term produced by turbulent fluctuations, and the overbar represents a short-hand average. The Boussinesq hypothesis relates the $\rho\overline{u_i' u_j'}$ to the mean velocity gradient.

$$\cdot -\rho\overline{u_i' u_j'}=\mu_t\left(\frac{\partial u_i}{\partial x_j}+\frac{\partial u_j}{\partial x_i}\right)-\frac{2}{3}\left(\rho k+\mu_t\frac{\partial u_k}{\partial x_k}\right)\delta_{ij} \tag{4}$$

In Equation (4), the variables μ_t and k denote the turbulent viscosity and turbulent kinetic energy (TKE), respectively.

The mixture model theory is used to model multiphase flows, where the phases move at different velocities but assume local equilibrium over short spatial length scales. The mixture model solves the mixture momentum equation and prescribes relative velocities to describe the dispersed phases. The mixture model assumes that both phases (i.e., liquid and vapour) are homogenous. The continuity and momentum equations for the mixture model are as follows.

$$\frac{\partial}{\partial t}\left(\rho_m\right)+\nabla\cdot\left(\rho_m\vec{v}_m\right)=0 \tag{5}$$

$$\begin{aligned}&\frac{\partial}{\partial t}\left(\rho_m\vec{v}_m\right)+\nabla\cdot\left(\rho_m\vec{v}_m\vec{v}_m\right)=\\&-\nabla p+\nabla\cdot\left[\mu_m\left(\nabla\vec{v}_m+\vec{v}_m^{\,T}\right)\right]+\rho_m\vec{g}+\vec{F}\end{aligned} \tag{6}$$

In Equation (5) and (6), $\rho_m=\alpha_v\rho_v+(1-\alpha_v)\rho_l$ is the density of the mixture, $\vec{v}_m$ mass-averaged velocity, $\vec{F}$ body force, $\mu_m=\alpha_v\mu_v+(1-\alpha_v)\mu_l$ the viscosity of the mixture and α_v is the volume fraction of vapour. The multiphase mass transfer (evaporation and condensation) is governed by the vapour transport equation as given below.

$$\frac{\partial}{\partial t}\left(\alpha_v\rho_v\right)+\nabla\cdot\left(\alpha_v\rho_v\vec{v}_m\right)=R_e-R_c \tag{7}$$

The mass transfer source terms R_e and R_c in Equation (8) and (9) are connected to the growth and collapse of the vapour bubbles, respectively. The volume fraction of vapour was solved by Schnerr and Sauer's model (Schnerr and Sauer 2001), implementing a simplified Rayleigh-Plesset equation, which ignores impact of bubble growth acceleration, viscous effects, and the surface tension force.

$$R_e=\frac{\rho_v\rho_l}{\rho_m}\alpha_v\left(1-\alpha_v\right)\frac{3}{\Re_B}\sqrt{\frac{2}{3}\frac{p_v-p}{\rho_l}} \tag{8}$$

$$R_c=\frac{\rho_v\rho_l}{\rho_m}\alpha_v\left(1-\alpha_v\right)\frac{3}{\Re_B}\sqrt{\frac{2}{3}\frac{p-p_v}{\rho_l}} \tag{9}$$

p_v is vapour pressure and $\Re_B$ is bubble radius given below.

$$\Re_B=\left(\frac{\alpha_v}{1-\alpha_v}\frac{3}{4\pi}\frac{1}{n_0}\right)^{1/3} \tag{10}$$

$$\frac{d\Re_B}{dt}=\sqrt{\frac{2}{3}\frac{p_b-p}{\rho_l}} \tag{11}$$

In Equation (11), the simplified Rayleigh-Plesset equation was used, neglecting the second-order terms and the surface tension force regarding the high level of the pressure difference where p_b is the bubble surface pressure.

2.1 Verification and Validation

The verification and validation studies were conducted, concerning the measurements of the sea trials and the cavitation observation, using a high-fidelity Sliding Mesh (SM) technique to facilitate a more detailed flow investigation in full-scale numerical analyses (Celik et al 2008). The Grid Convergence Index (GCI) analyses were performed at the design speed of 12 knots (Fr= 0.208), tuning the mesh resolution on both propeller and GRS blades, and in their near field. A systematic series of grid densities refined by a constant ratio, 2, was used to quantify the numerical uncertainty through validation and verification analyses. The total number of cells within various grid densities are 23.3M, 21.0M and 18.5M. In order to resolve high-gradient velocity normal to the boundaries, an adequate number of prism layers were used. The number of the layers is assigned as 8, 10 and 12 by the coarsest to the finest mesh, respectively. The results of GCI analyses, including *T*, *Q*, *P*P_D, *J* and *w*, are given in Table 2.

Table 2. Analysis of the Grid Convergence Index (GCI) performed at the ship's design speed of 12 knots (Fr= 0.208).

GCI	2-1
T (kN)	0.4%
Q (kN-m)	0.3%
P_D (kW)	0.4%
J	1.1%
w	0.7%

The mesh generation was conducted using the STAR-CCM+, employing a trimmer-type technique to generate a hexahedral type grid. The first grid size near the wall is set to 0.1 mm to ensure an average y^+ value of >30, and the surface mesh is shown in Fig. (4). Local mesh refinements were also employed at specific locations, such as bow and stern of the ship, rudder and propeller, and the free surface, to resolve the high-gradient flow, interaction and the wave.

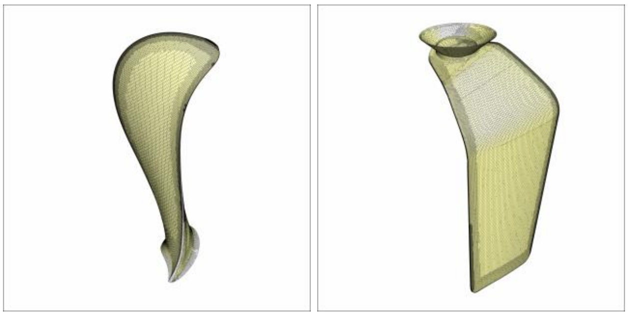

Figure 4. The surface mesh for the propeller and GRS blades.

A hull roughness survey was conducted (Ravenna et al 2021) in the dry dock, using a hull roughness gauge (TQC), to evaluate the ageing effect on the ship's performance, as the M/V ERGE has been in service for a decade. The average hull roughness (AHR) was calculated as 300 µm using mean hull roughness (MHR) measurement as below.

$$MHR = \frac{1}{10}\sum_{i=1}^{10} R_{t(50)i}, \quad AHR = \frac{1}{120}\sum_{j=1}^{120}\left(MHR\right)_j \qquad (12)$$

$R_{t\,(50)}$ is the mean gradient assessed by the microprocessor along the peaks and valleys for each of the 50 mm samples.

The added resistance due to the ageing effect was used to correct the measurements in sea trials, considering not only the roughness survey but also the model test results. Further details on the correction methodology of the ageing effect and model test extrapolation procedure are provided by Çelik et al (2022) and Çelik et al (2023), respectively. A comparison of the results obtained by the sea trials and the full-scale numerical analysis (CFD) is given in Table 3.

Table 3. The comparison of the sea trials and the numerical analysis (CFD) in the 8-degree configuration of GRS's blades.

Data	Trials	CFD	Δ (%)
N (RPM)	130.56	124.47	4.67
T (kN)	156.98	163.02	3.85
Q (kN-m)	82.623	82.830	0.25
P_D (kW)	1129.7	1079.7	4.43
σ	3.8397	4.2249	10.0
J	0.6064	0.5464	9.90
w	0.2305	0.3390	47.1

In Table 3, the estimation of thrust (T) and effective wake fraction (w) utilised the torque identity approach with torque coefficient (K_Q) as input data, while advance coefficient (J) and thrust coefficient (K_T) were derived from the propeller open water diagram. Results of the numerical analysis provide an agreement with the sea trials, as far as the propeller's speed (N), T, torque (Q) and delivered power (P_D) are concerned. Nevertheless, cavitation number (σ) and J deviates, and due to the cumulative errors arising by N and J, a remarkable discrepancy, 47.1%, is observed in the prediction of the w.

The volume fraction of the vapour (α_v) was assigned as 0.1% in the cavitation prediction, and the iso-contours to represent the vapour phase were extracted and overlaid with the footage captured by cavitation observation mechanism during the sea trials as shown in Fig. (5). V_S and N (hence, σ and J) were defined as the same as the sea trials for numerical analysis, enabling a direct comparison.

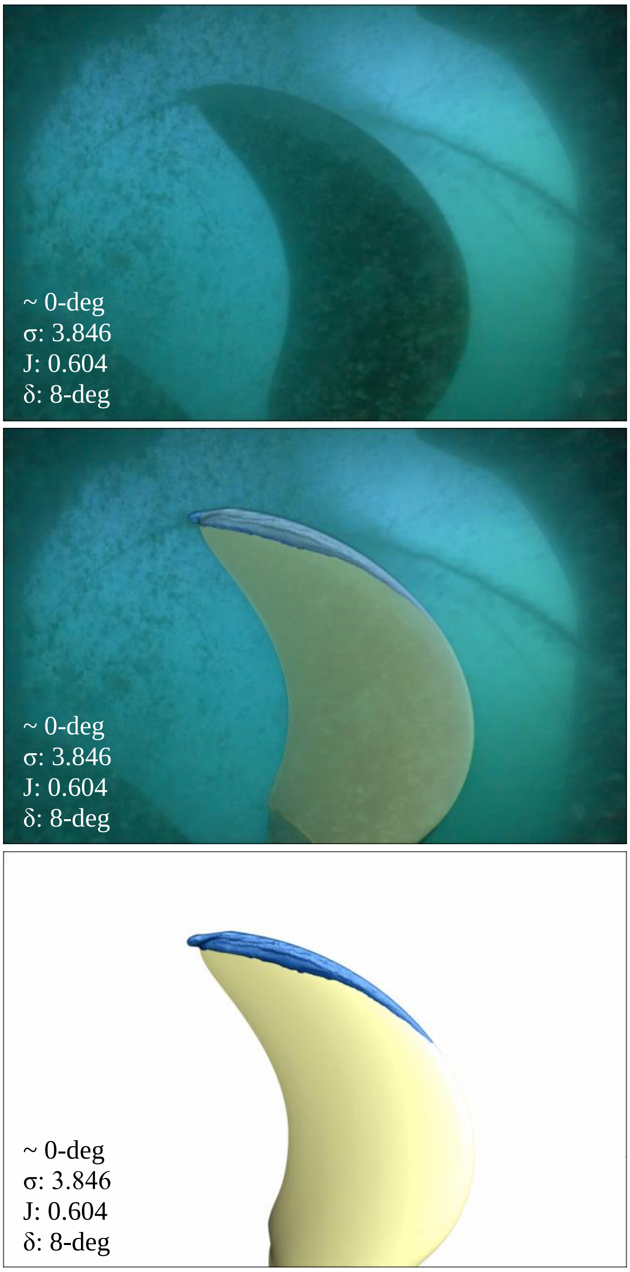

Figure 5. The comparison of the cavitation patterns obtained by the sea trials and the numerical analysis (CFD) at an approximately 0-degree angular position of a propeller blade.

In Fig. (5), a partial agreement is observed along the leading edge of the 0.75 r/R, extending towards the tip region, when comparing the cavitation pattern by the sea trials with the predictions obtained through full-scale numerical analysis (blue-coloured region in Fig. 5). On the other hand, the tip vortex cavitation extent could not be resolved accurately due to insufficient mesh resolution in the tip-vortex trajectory. A comparison of the cavitation patterns in varying angular positions (i.e., 0, 12, 24, 36, 48 and 60-degree) of a propeller blade is shown in Fig. (6). The cavitation phenomenon towards the blade tip region is in a solid form at the top dead centre position (i.e., 0-degree) of the propeller and turns into a weaker form, diminishing intensity as blade's angular position increases.

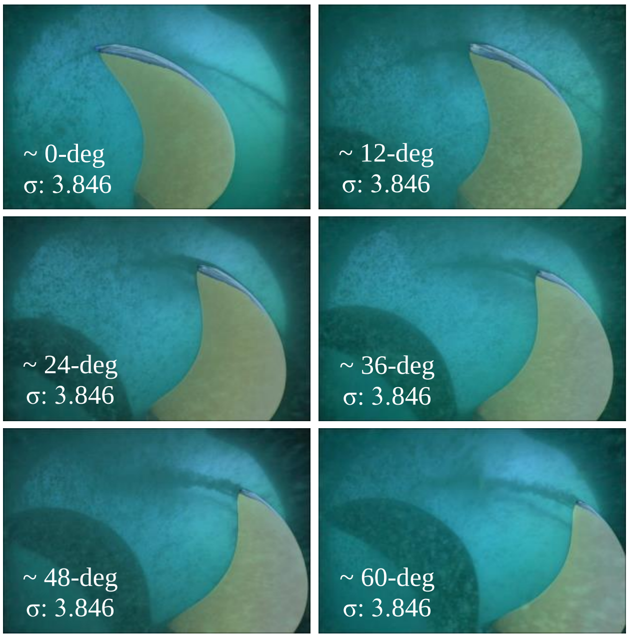

Figure 6. The comparison of the cavitation patterns obtained by the sea trials and the numerical analysis (CFD) in varying angular position (i.e., 12, 24, 36, 48 and 60-degree) of a blade.

2.2 Numerical Results

Following the verification and validation analyses, a comprehensive study was performed to assess the impact of varying deflection angles on the cavitation extent. In Fig. (7), the representation of the GRS toe-out angles (i.e., trailing edges of the rudders are getting closer) at 0, 5, and 8-degrees is illustrated. The self-propulsion points in each GRS configuration, and the corresponding propeller speed were detected at the ship's design speed (i.e., V_S= 12 knot).

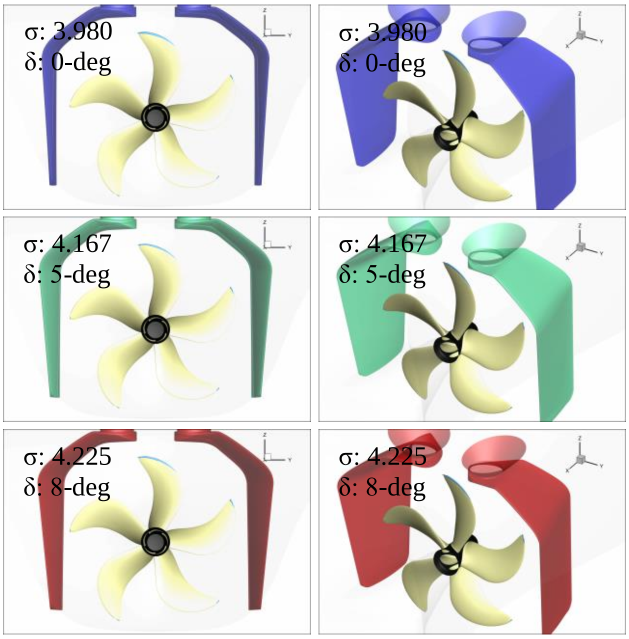

Figure 7. The representation of the GRS toe-out angles (trailing edges of rudders getting closer) at 0, 5, and 8-degree.

The results of the numerical analyses at the ship's design speed and in 0, 5, and 8-degrees of deflection/toe-out angle, including the N, T, Q, P_D, σ, J and w are given by Table 4.

Table 4. The results of the numerical analyses in varying GRS toe-out configurations, at 0, 5, and 8-degree deflection angles.

δ (DEG)	0	5	8
N (RPM)	128.24	125.33	124.47
T (kN)	162.90	160.00	163.02
Q (kN-m)	84.090	81.990	82.830
P_D (kW)	1129.3	1076.1	1079.7
σ	3.9801	4.1671	4.2249
J	0.5748	0.5619	0.5464
w	0.2836	0.3155	0.3390

As shown in Table 4, at the self-propulsion point (i.e., V_S= 12 kn), the propeller speed (N) decreases with increasing toe-out angle (δ). Nevertheless, in the 8-degree, both T and Q are greater than in the 5-degree, even if the N decreases due to the varying toe-out angle's impact on the V_A. The P_D decreases in the 5 and 8-degree configurations compared to the 0-degree, improving the energy efficiency. The σ decreases with increasing toe-out angle based on the N. The J decreases, and w increases in the influence of N and V_A as the toe-out angle increases. The impact of the toe-out angle on the cavitation is shown in a quantitative and qualitative manner in Fig. (8) and (9). A detailed investigation has yet to be presented, but the sea trials revealed the GRS influence on fuel consumption at various rudder angles, leading to adopt an δ: 8-degree rudder angle.

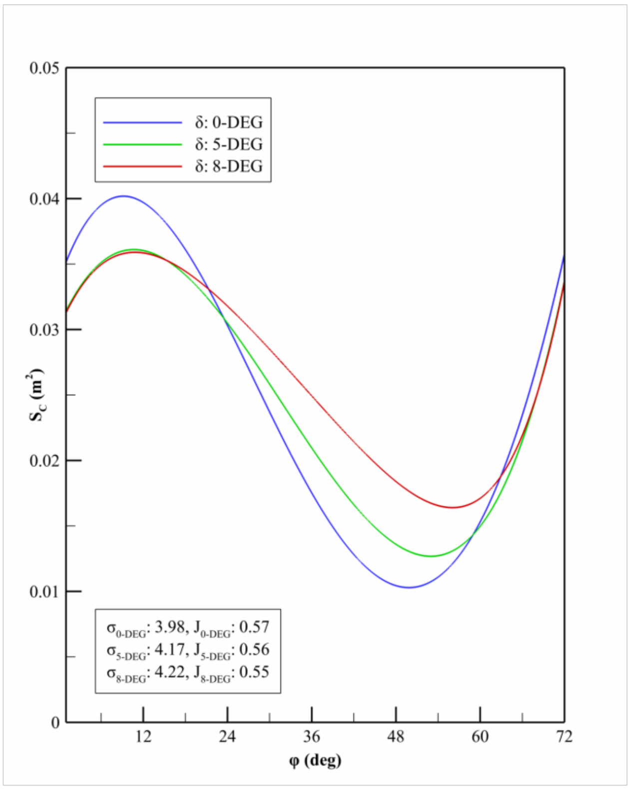

Figure 8. The fluctuation of the projected cavitation area (S_C) on the propeller blades at 0, 5, and 8-degree deflection angles.

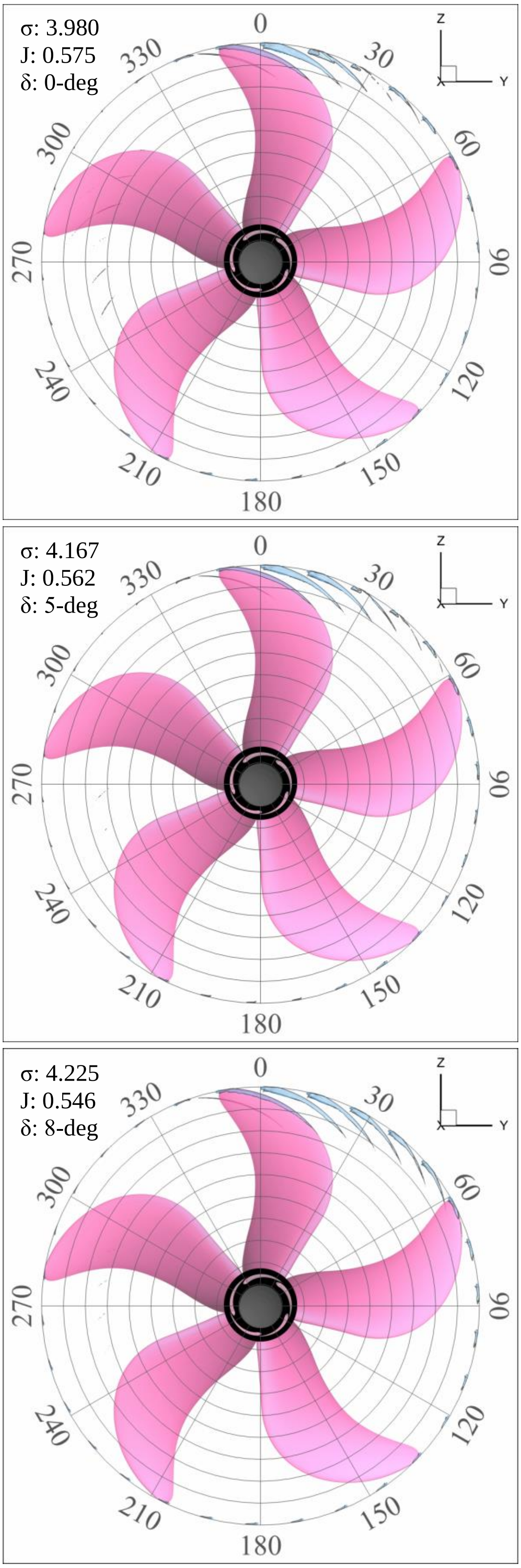

Figure 9. The cavitation patterns in the sequence of 12-degree angular blade positions at 0, 5, and 8-degree deflection angles.

In Fig. (8) and (9), the results of the numerical analyses in varying toe-out angles (i.e., trailing edges of the rudders are getting closer) indicate that the tip-vortex cavitation is apparent by -15 (i.e., 345-degree) to 90-degree of the propeller's blade angular position, and the cavitation pattern is negligible in the rest of the field. In all configurations, the pressure side of the propeller blades is entirely cavitation-free, and no hub vortex cavitation is observed. The findings align well with the model test results shown by Santic et al (2023) and GATERS (2023a).

The cavitation in wake shadow, through -15 to 15-degree (see Fig. 9 and 10), is solely dependent on the propeller's speed (*N*) due to not surround by the GRS's blades (see Fig. 11), and the deflection angle indirectly affecting cavitation.

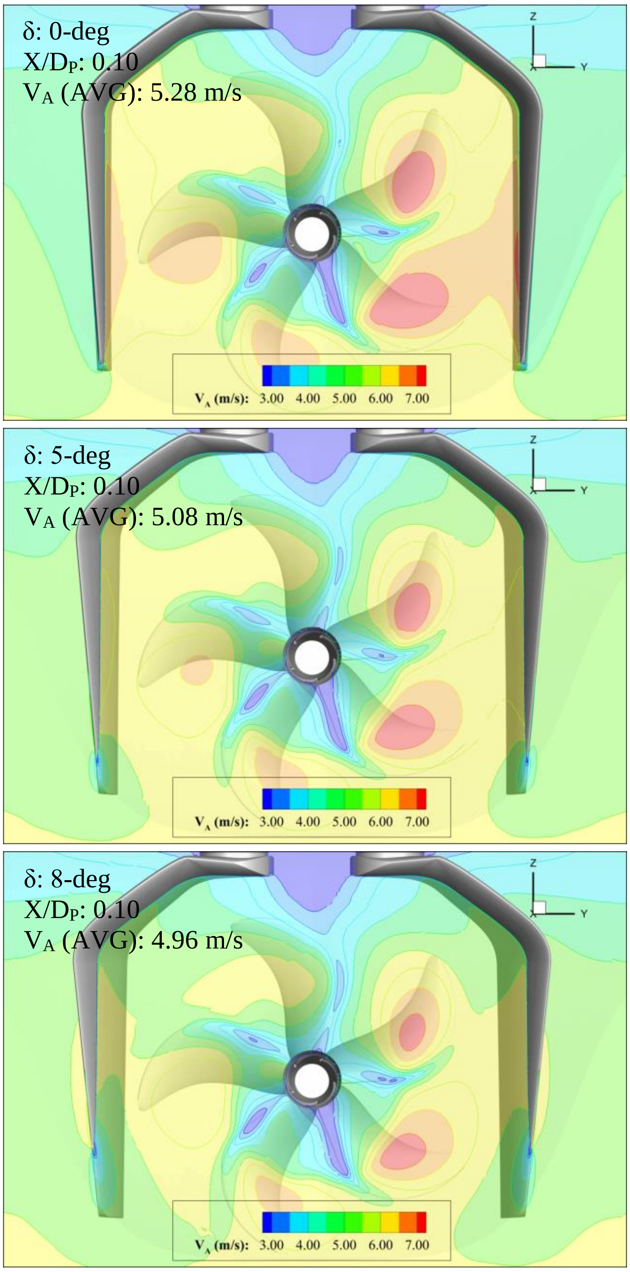

Figure 10. The advance speed (V_A) distributions along the sections extracted in upstream parallel to the propeller plane.

In Fig. (10), the expansion of the GRS's blades reduces the inflow velocity, excluding the wake shadow, due to its impact on both the propeller speed and the geometric form. Therefore, the majority of the cavitating field, through 15 to 90-degree, is directly affected by the GRS toe-out angle.

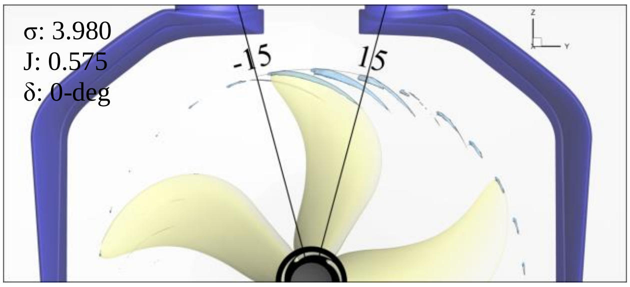

Figure 11. The cavitation pattern in the wake shadow, through a -15 to 15-degree of the propeller's angular position.

The averaged pressure coefficients, $C_P = (p - p_0)/(0.5\rho V_S^2)$, on horizontal sections through the GRS's blades at positions of r/R: 0.0, 0.5 and 1.0·D_P, are given in Table 5 at 0, 5, and 8-degree deflection/toe-out angle of the GRS.

Table 5. The average (AVG) pressure coefficients (C_P) of the GRS' port side and starboard side along the sections of r/R: 0.0, 0.5 and 1.0·D_P on the blade's pressure side (PS) and suction (SS) side at 0, 5, and 8-deg toe-out angles of the GRS.

C_P (AVG)	δ: 0-deg	δ: 5-deg	δ: 8-deg
PS (0.0·D_P)	0.447	0.368	0.247
SS (0.0·D_P)	-0.108	0.177	0.290
PS (0.5·D_P)	0.465	0.412	0.335
SS (0.5·D_P)	-0.081	0.195	0.301
PS (1.0·D_P)	0.455	0.414	0.359
SS (1.0·D_P)	0.210	0.327	0.375

In Table 5, C_P decreases with an increase in the toe-out angle (i.e., by 0 to 8-degree) on the pressure side, while on the suction side, C_P increases with an increase in the toe-out angle. In positions of 0.5·D_P and 1.0·D_P on the pressure side, C_P coefficients are in a similar trend and higher than in positions of 0.0·D_P, while on the suction side, C_P coefficients are in reasonable agreement in positions of 0.0·D_P and 0.5·D_P but lower than in positions of 1.0·D_P. The overall difference in C_P coefficients (ΔC_P) between the pressure side (PS) and suction side (SS) is maximum at the 0-degree configuration. The ΔC_P is similar at 5- and 8-degree configurations but lower than observed at 0-degree.

The pressure coefficient distribution along the chord by the trailing edge (x/c: 0) to the leading edge (x/c: 1) on the GRS' port side and starboard side blades' suction side and pressure side sections (r/R: 0.0, 0.5 and 1.0) at 0, 5, and 8-degree configurations of the GRS are given in Fig. (12), (13), (14) and (15). The change in toe-out angle leads to the change in the pressure distribution along the GRS' blades. So, this difference leads to a negative pressure coefficient at 0-degree configuration by the x/c: 0.6 to x/c: 1.0 on the suction side. However, no flow separation or cavitation was observed on the blades in any configuration.

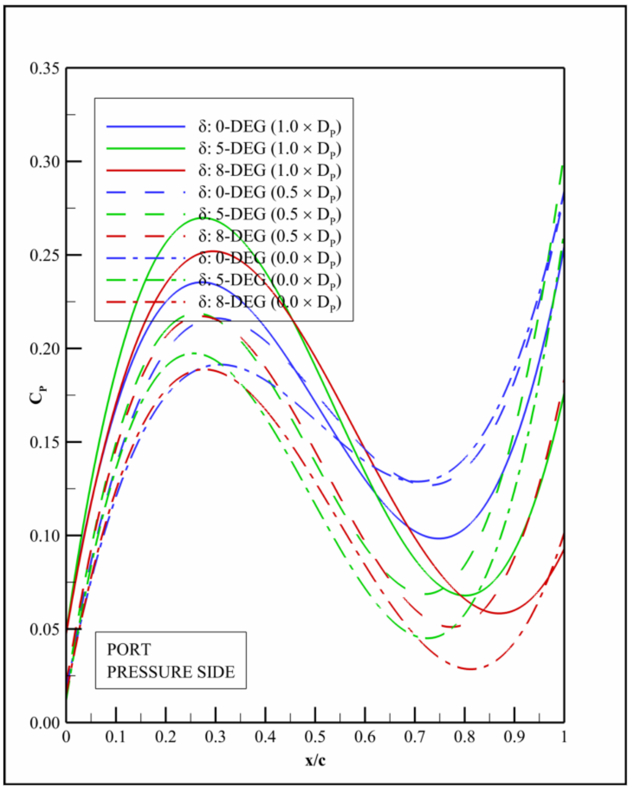

Figure 12. The pressure coefficient (C_P) distribution along the chord by the trailing edge (x/c: 0) to the leading edge (x/c: 1) on the GRS' port side blade's pressure side sections (r/R: 0.0, 0.5 and 1.0) at 0, 5, and 8-degree deflection angles of the GRS.

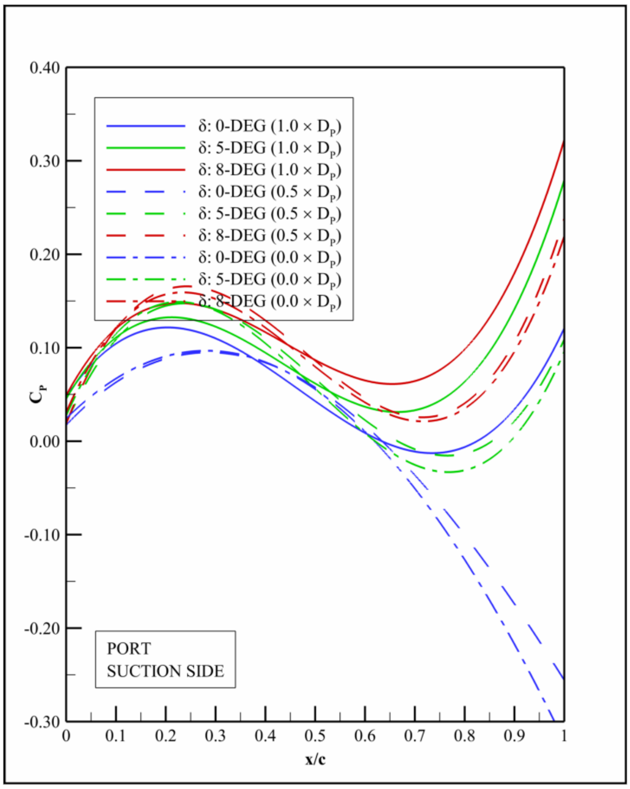

Figure 13. The pressure coefficient (C_P) distribution along the chord by the trailing edge (x/c: 0) to the leading edge (x/c: 1) on the GRS' port side blade's suction side sections (r/R: 0.0, 0.5 and 1.0) at 0, 5, and 8-degree deflection angles of the GRS.

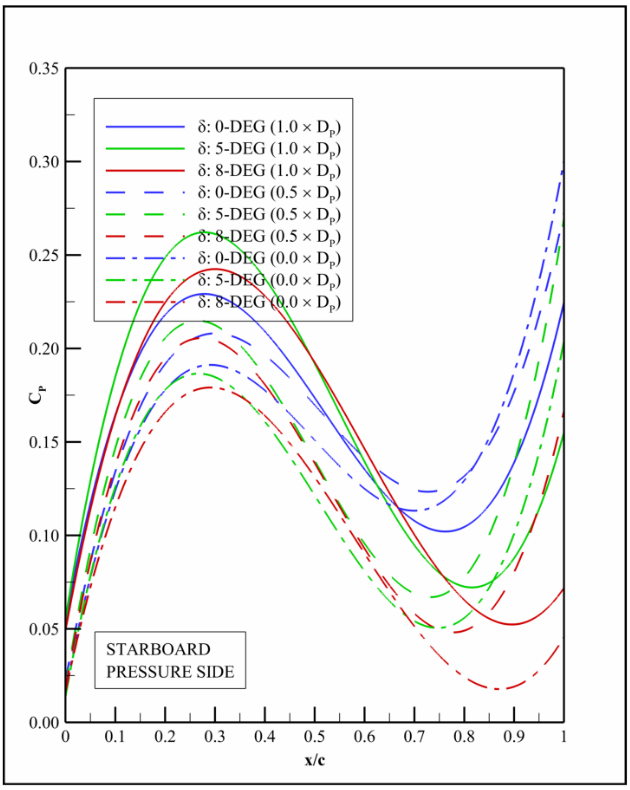

Figure 14. The pressure coefficient (C_P) distribution along the chord by the trailing edge (x/c: 0) to the leading edge (x/c: 1) on the GRS' STB side blade's pressure side sections (r/R: 0.0, 0.5 and 1.0) at 0, 5, and 8-degree deflection angles of the GRS.

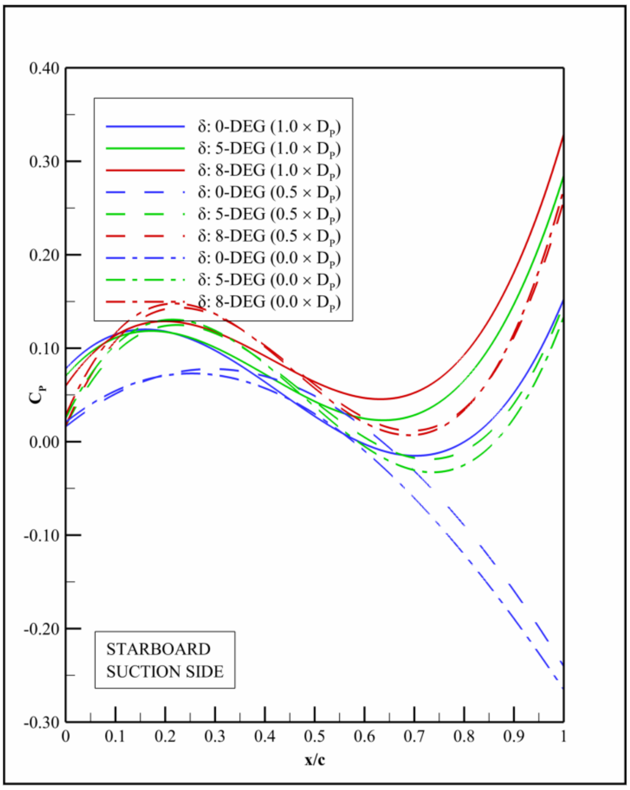

Figure 15. The pressure coefficient (C_P) distribution along the chord by the trailing edge (x/c: 0) to the leading edge (x/c: 1) on the GRS' STB side blade's suction side sections (r/R: 0.0, 0.5 and 1.0) at 0, 5, and 8-degree deflection angles of the GRS.

3 CONCLUSIONS

The study is on the assessment of the numerical analyses concerning the sea trials to address the impact of the rudder angle(s) variations on the GRS propeller's cavitation, driven by a number of time-dependent CFD simulations. The findings of the study lead to the following conclusions.

- A well-equipped and organised mechanism to observe the cavitation phenomenon in sea trials brings the benefits of in-detail cavitation investigation, enabling enhancements in the design and providing a reference.
- In the numerical analyses, cavitation extent is slightly misrepresented compared to the sea trials, but the predictions along the full-scale simulations are substantially reliable due to the uncertainties in trials and the definition of flow characteristics in simulation.
- One may refer to the GRS as an open duct based on the phase-averaged inflow velocity (V_A) distribution along the section extracted upstream parallel to the propeller plane, and the prediction of the cavitation along the wake shadow area in varying toe-out angles.
- The GRS' impact, reducing the power consumption, may also be attributed to its interaction with the hull and propeller rather than solely to the added thrust provided by the GRS blades due to ΔC_P and P_D being maximum at the 0-degree compared to 5 and 8-degree.
- The study revealed that the rudder angle configuration of the GRS influences not only the performance but also the cavitation due to its obvious impact on the self-propulsion point, and effective wake fraction (w).
- The impact of the toe-out angle on cavitation is to be assessed by resolving the tip-vortex cavitation in full-scale analyses. This involves improving mesh quality, implementing an adaptive mesh refinement technique.

The first GRS application in Europe and the first global GRS retrofit application ever, M/V ERGE has been in operation for up to nine months now. The ship's crew experience, relying on the voyage data, shows that the GRS's optimum deflection angle may vary depending on the ship's draft and the sea state. Notably, the GRS's contribution to energy efficiency in rough sea conditions is even better compared to a conventional rudder system (CRS). As a further study, comprehensive numerical analyses are to be performed on the seakeeping performance of the GRS and the CRS to assess the impact of the rudder blade's dynamics to keep the ships on course.

ACKNOWLEDGEMENTS

This paper is based on the activities conducted in the collaborative European project GATERS which is an Innovation Action Project funded by the European Commission (EC) H2020 Programme (ID: 860337) with independent aims and objectives. The project has an official sub-license agreement with Wartsila Netherlands BV to utilise the Gate Rudder Patent (EP 3103715) at specific retrofit projects of vessel sizes below 15000 DWT. The authors extend special thanks to Mr Metin Şener of CAPA DENIZCILIK for his valuable contribution and support in conducting the observations during the sea trials.

REFERENCES

Blazek, J. (2001). 'Computational Fluid Dynamics: Principles and Applications'. Elsevier. Oxford, UK

Carchen, C., Turkmen, S., Piaggio, B., Shi, W., Sasaki, N. and Atlar, M. (2021). 'Investigation of the manoeuvrability characteristics of a Gate Rudder system using numerical, experimental, and full-scale techniques'. Applied Ocean Research, Volume 106.

Celik, I.B., Ghia, U., Roache, P.J., Freitas, C.J., Coleman, H. and Raad, P.E. (2008). 'Procedure for estimation and reporting of uncertainty due to discretization in CFD applications'. Journal of Fluids Engineering.

Çelik, C., Özsayan, S., Köksal, Ç.S., Danışman, D.B., Korkut, E., and Gören, Ö. (2022). 'On the Full-Scale Powering Extrapolation of Ships with Gate Rudder System (GRS)'. A. Yücel Odabaşı Colloquium Series 4th International Meeting - Ship Design & Optimization and Energy Efficient Devices for Fuel Economy. Istanbul, Türkiye.

Çelik, C., Özsayan, S., Köksal, Ç.S., Danışman, D.B., Korkut, E., Gören, Ö. and Atlar, M. (2023). 'On the Evaluation of the Model Test Extrapolation by Sea Trial Measurements'. 7th International Conference on Advanced Model Measurement Technology for the Maritime Industry. Istanbul, Türkiye.

Gate Rudder System as a Retrofit for the Next Generation Propulsion and Steering of Ships (2023a). 'Scaled Model Tests Conducted in Task 1.3'. The EC - H2020 Project GATERS. Work Package 1.

Gate Rudder System as a Retrofit for the Next Generation Propulsion and Steering of Ships (2023b). 'Dedicated on-board sea trials of the target ship before and after the GRS retrofit'. The EC - H2020 Project GATERS. Work Package 2, D2.2.

Gate Rudder System as a Retrofit for the Next Generation Propulsion and Steering of Ships (2024). 'Voyage monitoring of target ship with the CRS and GRS'. The EC - H2020 Project GATERS. Work Package 2, D2.1

Gürkan, A.Y., Ünal, U.O., Aktas, B. and Atlar, M. (2023a). 'An investigation into the gate rudder system design for propulsive performance using design of experiment method'. Ship Technology Research (Schiffstechnik).

Gürkan, A.Y., Ünal, U.O., Aktas, B., Köksal, Ç.S. and Atlar, M. (2023b). 'Comprehensive Investigation of the Form Design of The Gate Rudder for Propulsive Performance Using Design of Experiment Method'. 25th Numerical Towing Tank Symposium. Ericeira, Portugal.

Köksal, Ç.S., Aktas, B., Gürkan, A.Y., Korkut, E., Sasaki, N. and Atlar, M. (2022). 'Experimental Powering Performance Analysis of M/V ERGE in Calm Water and Waves'. A. Yücel Odabaşı Colloquium Series 4th International Meeting - Ship Design & Optimization and Energy Efficient Devices for Fuel Economy. Istanbul, Türkiye.

Köksal, Ç.S., Gürkan, A.Y., Aktas, B., Ünal, U.O., Fitzsimmons, P., Sasaki, N. and Atlar, M. (2023a). 'Cavitation Observation of M/V ERGE During the Sea Trials: A Comparison of Gate Rudder and Conventional Rudder Configurations'. 7th International Conference on Advanced Model Measurement Technology for the Maritime Industry. Istanbul, Türkiye.

Köksal, Ç.S., Gürkan, A.Y., Aktas, B., Turkmen, S., Zoet, P., Sasaki, N. and Atlar, M. (2023b). 'Underwater Radiated Noise Measurements of Pre- and Post-Retrofit of Gate Rudder System During the Sea Trials'. 7th International Conference on Advanced Model Measurement Technology for the Maritime Industry. Istanbul, Türkiye.

Köksal, Ç.S., Gürkan, A.Y., Aktas, B., Sasaki, N. and Atlar, M. (2023c). 'Influence of Gate Rudder System (GRS) Rudder Angle(s) on the Propulsive Efficiency'. 25th Numerical Towing Tank Symposium. Ericeira, Portugal.

L. Davidson, L. (2005). 'Numerical Methods for Turbulent Flow, MTF071 Lecture Notes'. Chalmers University of Technology: Department of Thermo and Fluid Dynamics. Goteborg, Sweden.

Özsayan, S., Aydın, C., Köksal, Ç.S., Ünal, U.O. and Korkut, E. (2023). 'Effects of the Gate Rudder System (GRS) on the Experimental Cavitation Observations and Noise Measurements'. 7th International Conference on Advanced Model Measurement Technology for the Maritime Industry. Istanbul, Türkiye.

Patankar, S.V. and Spalding, D.B. (1972). 'A Calculation Procedure for Heat, Mass and Momentum Transfer in Three-Dimensional Parabolic Flows'. International Journal of Heat and Mass Transfer 15, 1787-1806.

Ravenna, R., Köksal, Ç.S. and Atlar, M. (2023). M/V ERGE's Hull Fouling and Roughness Survey Report. The EC - H2020 Project GATERS.

Santic, I., Mauro, S., Micci, G. and Felli, M. (2023). 'Systematic Experimental Survey of Propulsive and Acoustic Performances of a Gate Rudder System in Relation to a Conventional Rudder'. 7th International Conference on Advanced Model Measurement Technology for the Maritime Industry. Istanbul, Türkiye.

Sasaki, N., Kuribayashi, S. and Miles, A. (2019). 'Full scale performance of gate rudder'. Propeller & Impellers - Research, Design, Construction & Application.

Schnerr, G.H. and Sauer, J. (2001). 'Physical and numerical modeling of unsteady cavitation dynamic'. 4th International Conference on Multiphase Flow. New Orleans, USA.

Tennekes, H. and Lumley, J.L. (1972). 'A First Course in Turbulence'. MIT Press. Cambridge, UK.